GLYPH- AND TEXTURE-BASED VISUALIZATION OF SEGMENTED TENSOR FIELDS

Cornelia Auer, Claudia Stripf, Andrea Kratz and Ingrid Hotz
Zuse Institut Berlin, Takustrasse 7, 14195 Berlin, Germany

Keywords: Tensor Field Visualization, Texture Mapping, Glyph Placement.

Abstract: In this work we show how the variability of visualization methods like textures and glyphs can be used to enhance established methods like topology. A topology-based segmentation (Auer et al., 2011) serves as framework to map textures and place glyph exponents for two dimensional symmetric tensor fields. The textures encode physical properties of the underlying field and support the understanding of the field as a whole, whereas the glyph exponents can be used to give detailed insight at distinctive locations.

1 INTRODUCTION

Where to Place which Information and how? This is a crucial question even experts in visualization are permanently confronted with. An incomplete view is as undesirable as a cluttered image. Topological methods have a long tradition and for domain experts they serve as visualization itself. However, for untrained users this might be too abstract – especially if the visualization is meant to support a first understanding of the data. In this work, we exploit the topology-based segmentation of a two-dimensional tensor field (Auer et al., 2011) as basis for texture generation, as well as for the placement of glyphs.

Textures are a powerful tool to design continuous visualizations. They offer many parameters that can be used to encode features of interest. This makes textures especially interesting for the visualization of tensor fields. Tensor fields contain directional and scalar features which can be encoded in texture parameters. One challenge for many texture-based methods is the definition of appropriate texture coordinates. This is accomplished by the cells of the topology-based segmentation; they serve as consistent framework for the texture mapping. A dense visualization of the underlying tensor field can be generated using every pixel of the image to convey physical properties of the field. Furthermore, a diversity of visualization options arises: To encode directional information, for example, stripe patterns can be used; but also knitting or basketwork patterns are presented and evaluated towards their applicability to depict central tensor properties within the segmentation framework. The goal hereby is not to display all possible features in one image but to offer a flexible framework to a user to switch views for the different points of interest.

The placement of glyphs is an intricate topic for vector as well as tensor visualization. Here, we use the tensor field segmentation to display glyphs at distinctive locations in the given cells. The advantages of the global structural information provided by the topology and the detailed depiction of representative tensors via glyphs are combined in a single image.

Tensors are of interest in many application fields, for example, engineering, physics but also computer graphics. Especially for tensors in physics and engineering, even for two dimensional fields, the development of expressive visualizations is still an ongoing research topic. We will demonstrate our results for stress tensors which are of high importance in mechanical engineering.

2 RELATED WORK

The focus of this review is on visualization methods designed for tensor fields arising in applications such as physics and mechanical engineering. In general, the developed visualization methods can be subdivided into local and continuous methods.

Local Methods. Local methods use geometric objects (glyphs) to depict single tensors at discrete points. Shape, size, color, and texture can be used to encode tensor properties. The most common glyph

Auer C., Stripf C., Kratz A. and Hotz I..
GLYPH- AND TEXTURE-BASED VISUALIZATION OF SEGMENTED TENSOR FIELDS.
DOI: 10.5220/0003857106700677
In *Proceedings of the International Conference on Computer Graphics Theory and Applications* (IVAPP-2012), pages 670-677
ISBN: 978-989-8565-02-0
Copyright © 2012 SCITEPRESS (Science and Technology Publications, Lda.)

for tensors is an ellipsoid alligned to the tensor's eigenvectors and scaled according to its eigenvalues (Figure 1). Beside the design of glyphs (see (Hashash et al., 2003) for an overview of glyphs for stress and strain tensors), perceptional issues such as visual ambiguity need to be solved (Schultz and Kindlmann, 2010) when using glyphs for visualization. Another challenge is the placement of glyphs to maximize the information that is conveyed in an image. Previous methods in this context aimed to create sample distributions that avoid holes and overlaps (Kindlmann and Westin, 2006), (Hlawitschka et al., 2007), (Feng et al., 2008), (Kratz et al., 2011). In this work, we address the question where to place glyphs by exploiting a segmentation of the tensor field.

Continuous Methods. Closely related to our work are texture-based methods, which are motivated by vector field visualization. Line integral convolution (LIC) (Cabral and Leedom, 1993), for example, has been extended to HyperLIC (Zheng and Pang, 2003). It uses a multi-pass approach to represent the orientation of one eigenvector field and to highlight anisotropy. Another extension are fabric textures (Hotz et al., 2004). Two LIC images for every eigenvector field are computed and blended, which leads to an image that resembles a fabric encoding central physical properties of stress tensor fields into fiber thickness (thin = compression, thick = expansion). Recently, a novel method based on anisotropic sampling was introduced (Kratz et al., 2011). By computing a generalized Voronoi diagram on the basis of a tensor-determined local metric, the resulting regions can be texturized which results in a large variety of possibilites to create visualizations. In general, texture-based methods are restricted to two-dimensional surfaces.

Three-dimensional visualization methods for stress tensor fields are rare (Dick et al., 2009), (Kratz et al., 2011). They focus on hybrid methods to emphasize interesting regions and to avoid clutter. When features of interest are not known in advance, explorative methods can help (Kratz et al., 2011). To depict the behavior of a single eigenvector field, tensorlines can be used. These are defined as lines that are tangential to the chosen eigenvector field. Hyperstreamlines (Delmarcelle and Hesselink, 1993) are an extension, which additionally incorporate the eigenvalues and other principal directions.

Topological Methods. Tensor fields can also be represented by extracting their topology, which is represented by a graph structure. This *topological graph* consists of degenerate points and connecting tensorlines (Delmarcelle, 1994), (Lavin et al., 1997), which separate the field into regions of similar eigenvector behavior. Simplification and tracking of the graph (Tricoche et al., 2001) results in a structure that is easier to understand and enhances their practical applicability. This paper builds on a topological segmentation (Auer et al., 2011). Therefore, the topological graph is extracted (Sreevalsan-Nair et al., 2010) and recursively refined according to eigenvalue characteristics. Thus, a segmentation of the field is achieved that accounts for both, eigenvalue and eigenvector behavior. Work that is concerned with topology extraction for three-dimensional fields is rare (Hesselink et al., 1997), (Zheng and Pang, 2004), (Tricoche et al., 2008).

3 BASICS AND NOTATION

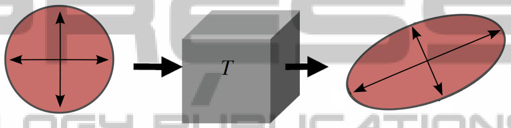

Figure 1: Illustration of the tensor concept: result (ellipse) of applying a tensor to an isotropic element (sphere). The resulting eigenvectors are depicted as arrows and the eigenvalues are reflected by the scaling of the arrows.

SCITEPRESS SCIENCE AND TECHNOLOGY PUBLICATIONS

3.1 Tensors

This work focuses on the visualization of two-dimensional symmetric tensors. For a fixed coordinate system in $\mathbb{R}^2$ such a tensor can be described as 2×2 matrix of real numbers. For the remainder of this paper, if not stated differently, the word tensor refers to two-dimensional symmetric tensors.

Eigenvalues $\lambda_i \in \mathbb{R}$ and eigenvectors $\overset{\leftrightarrow}{v_i} \in \mathbb{R}^2$, with $i = 1, 2$ are important invariants of a tensor. They are defined by the *characteristic equation* $\mathbf{T} \cdot \lambda_i = \overset{\leftrightarrow}{v_i} \cdot \lambda_i$. The eigenvectors specify the direction of extremal variation of the quantity encoded by the tensor; the eigenvalues give the magnitude of those extremal variations (Figure 1). For symmetric tensors the eigenvalues are real and the eigenvectors mutually orthogonal. The double arrows allude to the fact that eigenvectors are bidirectional. A tensor is fully represented by its eigenvectors and eigenvalues. In the following the eigenvalues are ordered such that $\lambda_1 \geq \lambda_2$. They are called *major* respectively *minor* eigenvalues with associated major and minor eigenvector.

3.2 Tensor Fields

A tensor field assigns a tensor to each point in a domain. In our case the input tensor fields are given on a triangulated planar domain, where each vertex of the triangulation is assigned to a tensor. The tensor fields are decomposed into to two eigenvector- and two eigenvalue fields (major resp. minor). Integral-lines that are tangential to an eigenvector field everywhere are called *tensorlines*. To distinguish whether the tensorlines belong to the major or the minor eigenvector field, a color-coding is used: *blue* refers to the minor field and *red* to the major field.

3.3 Topology

The topology is represented by the *topological graph*, which consists of *degenerate elements* and *separatrices*. Degenerate elements are locations where both eigenvalues are equal, λ_1=λ_2, and thus the eigenvectors $\overset{\leftrightarrow}{v_i}$ are not uniquely defined. Mostly they occur as points but also as elements of higher dimensionality, such as lines. Separatrices are distinctive tensorlines, that radially emerge from degenerate elements and bound sectors of homogeneous eigenvector behavior. For more details we refer to (Delmarcelle and Hesselink, 1993).

4 TOPOLOGICAL SEGMENTATION

This work builds on a refined topological graph yielding a complete segmentation of the tensor field (Auer et al., 2011). This segmentation returns cells with homogeneous eigenvector and eigenvalue behavior. Starting point for the segmentation is the *integral topological graph* combining the topology of both eigenvector fields. As the eigenvector fields are orthogonal to each other this graph segments the tensor field into curvilinear cells of homogeneous eigenvector behavior (Figure 2(a)). Eigenvalues are used to iteratively adapt the topological cells until they fulfill predetermined resolution, accuracy, and uniformity criteria (Figure 2(b,c)). If a cell exhibits dissimilarity above a predefined accuracy threshold, it gets split by starting a subdividing tensor line. Further, neighboring cells that are homogeneous get merged by deleting the connecting edge. To steer the similarity of eigenvalue characteristics within a cell, one or more expressive scalar fields are defined. These can be the eigenvalues, but also derived tensor invariants. For stress tensor fields, e.g., quantities of special interest arise in context with failure analysis. Exemplary we use *relative shear* τ_R and *maximum shear stress* τ as anisotropy measures.

$$\tau = |\lambda_1 - \lambda_2| \text{ , and } \tau_R = \frac{|\lambda_1 - \lambda_2|}{\sqrt{\lambda_1^2 + \lambda_2^2 + A^2}} \; , \qquad (1)$$

where $A \in \mathbb{R}$ is a positive constant.

The resulting cells are bounded by tensorlines and possibly degenerated lines. The integration of the tensor lines using a Runge-Kutta-4th-order integration scheme yields a representation of tensorlines as polylines. Adaptive step sizes are used to maximize the accuracy of this numerical integration scheme.

5 VISUALIZATION METHOD

In this work we build upon the results of the segmentation (Section 4) and extend it to a texture- and glyph-based visualization. Mapping textures into the segmented cells yields a continuous rendering of the tensor field. This facilitates a comprehension of the field's global nature. The glyph-based approach combines the advantages of the global structural information provided by the topology and the local detailed view of representatives via glyphs.

Cell Structure. Cells that are not adjacent to degenerate points or the domain boundary are quadrangular and bounded by two major and minor tensorline segments in alternating order (Figure 2(c),(d)). Other cells can have more general shapes. The boundaries of the extracted cells are stored as polylines (Figure 3).

Preprocessing. As mentioned in Section 4, the bounding tensorlines are computed by an integration scheme with adaptive step size. This guarantees accurate results in the segmentation process but leads to irregular distances between the vertices of the polylines. To obtain good results for the texturing and glyph locations, however, a more uniform sampling of the cell boundaries is favorable. This is achieved by a pre-processing step deleting respectively adding vertices if the distance to adjacent vertices does not fall in a pre-defined distance interval. An angle criterion guarantees that tensorlines are still sufficiently aligned with the eigenvector fields.

For the texture mapping the segmented cells need to be triangulated. We use a constrained Delaunay triangulation that maintains non-convex shape.

All pre-processing steps only have to be performed once after the segmentation process.

Eigenvalue Mapping. The goal of this work are intuitive visualizations of stress tensors. These, in general, are not positive definite and thus, have positive as well as negative eigenvalues. We will use the eigenvalues to control basic texture parameters such as texture density. Therefore the eigenvalues are mapped

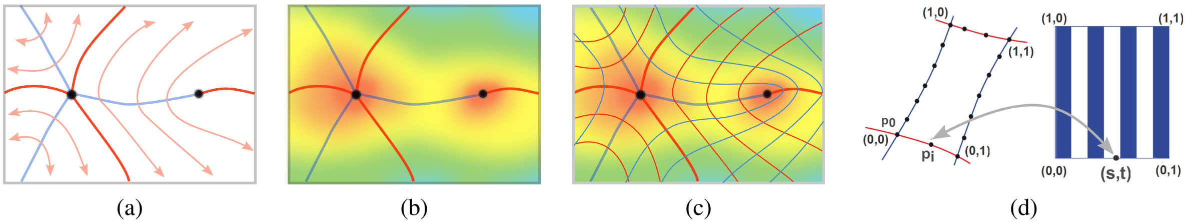

(a) (b) (c) (d)

Figure 2: (a-c) Schematic illustration of the segmentation process. (a) Step 1: Integral topological graph with degenerate points as black dots, separatrices as bold lines (major in red, minor in blue). The light red lines depict tensorlines within the segmented regions and exemplarily illustrate how separatrices aggregate homogeneous eigenvector behavior. (b) Step 2: Definition of scalar field. (c) Step 3: Refinement of topological graph according to scalar field. (d) Texturization of segmented cell. Mapping of point p_i to texture coordinate (s,t) in quadrangular cell.

into a restricted positive interval. We adopt a mapping that simulates a texture deformation generated by the underlying tensor field (Hotz et al., 2004). Thus, negative eigenvalues (compression) lead to dense and positive eigenvalues (expansion) to sparse textures. Hotz et al. define:

$$F(\lambda) = a + \sigma \cdot f(\lambda)\ . \qquad (2)$$

The function f is chosen to have a large slope in the neighborhood of zero. In this work, f is the hyperbolic tangent, which preserves the differentiation of negative and positive eigenvalues. The parameter a relates to an offset and σ is an additional scaling factor for the slope. Both can be adjusted by the user.

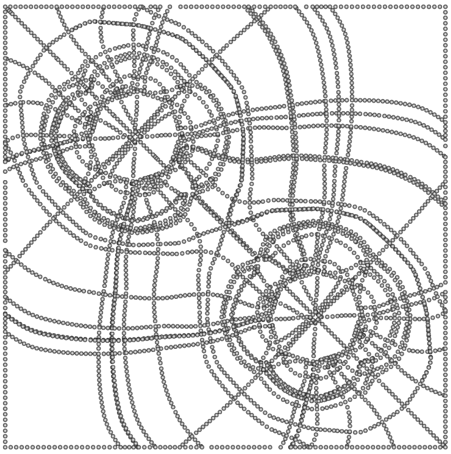

Figure 3: Result of a segmentation, points of the cell bounding polylines are depicted as spheres.

5.1 Segmentation-based Glyph Placement

The characteristics of the tensor field – the eigenvectors and eigenvalues – are similar inside each extracted cell (Section 4). Thus, the essential tensor properties of each cell can be visualized by one representative glyph. The task is to find an appropriate position within each cell to place this representative. Since most of the segmented cells are non-convex we follow an algorithm for the computation of *barycentroids* of arbitrarily shaped planar polygons (Rustamov et al., 2009). This algorithm is based on an *interior distance* measure. The barycentroid is defined as the point with minimal average interior distance to the boundary points. Finding this point is a convex optimization problem and can be solved by standard gradient descent routines. The barycentroid has the characteristic that it captures the *semantic center* of the polygon and lies inside any arbitrary shaped planar polygon. See Figure 5 for results.

5.2 Segmentation-based Texturization

Using the segmented cells as basis for texturization has several benefits. The cells inherently provide the parametrization for the texture mapping and the underlying topology ensures structural correctness.

Also the segmented cells bounded by tensorlines already give the eigenvector directions. Simple procedural stripe textures already depict one eigenvector field. Thus, the use of textures with one or two orthogonal dominant directions results in continuous representations of the correct eigenvector behavior within these cells (Figure 4). But also more sophisticated textures, like knitting patterns, lead to expressive representations (Figure 7). The density of the texture pattern will also be used to reflect physical properties of the tensor field, such as compression and expansion (e.g. Figure 4(b)).

Cells containing degenerate elements in their boundary can have more complex shapes and the eigenvector behavior cannot be easily represented by simple stripe patterns. In addition, in the proximity of degenerate elements the eigenvector behavior is weakly expressed. For such cells two options are provided. Either these cells are skipped or textured with an isotropic noise pattern encoding information about the isotropic eigenvalues.

SCITEPRESS SCIENCE AND TECHNOLOGY PUBLICATIONS

For one-directional textures, as stripe patterns, one image per eigenvector field is computed. To depict both eigenvector fields in one image the results for each field are blended (Figures 4(c), 6).
The texturization is performed by vertex and fragment shaders. Texture coordinates (s,t), with $s,t \in [0,1]$ for quadrangular cells are initially computed by mapping the points of a cell boundary to a unit square (Figure 2(d)).

5.2.1 Rendering of Eigenvector Directions

All methods that are presented in the following are based on textures with linelike elements to depict directions. To ensure that the cell size does not affect the perception of the pattern, we need a special mapping approach that provides an approximately constant pattern frequency (Hummel et al., 2010)(Figure 4(a)). Hummel et al. adjust the sampling frequency according to the image-space partial derivatives η_s, η_t at pixel (i,j) of the texture coordinate (s,t):

$$\begin{aligned} \eta_s(i,j) &= \sqrt{\left(\frac{\delta s}{\delta i}\right)^2 + \left(\frac{\delta s}{\delta j}\right)^2}\,, \\ \eta_t(i,j) &= \sqrt{\left(\frac{\delta t}{\delta i}\right)^2 + \left(\frac{\delta t}{\delta j}\right)^2}\,. \end{aligned} \tag{3}$$

The initial texture coordinates (s,t) remain unchanged. The evaluation of the input texture P is modified according to the variation of η_s and η_t and steers the pattern frequency in the final image. $\hat{P}_{l_s,l_t}$ gives the frequency adjusted texture values

$$\hat{P}_{l_s,l_t}(s,t) := P(s \cdot 2^{-l_s}, t \cdot 2^{-l_t})\,, \tag{4}$$

with $l_s = \log_2 \eta_s$ and $l_t = \log_2 \eta_t$. Hence, short edges with high partial derivatives yield a low pattern frequency. For large edges this works vice versa. The resulting pattern frequency also interactively adjusts to the current zoom level and resolution of the image. As resolution levels are discretely defined values for neighboring resolution levels are computed and bilinear filtering applied to achieve a smooth pattern frequency. The evaluation of Equation 3 can be done by built-in functionality of the rendering system.

5.2.2 Rendering of Eigenvalue Characteristics

Line Frequency. The approach of Hummel et al. (Hummel et al., 2010) serves as basis to encode physical properties like compression and expansion by the pattern frequency (Figure 4(b)). This is achieved by replacing Equation 3 by the following:

$$\begin{aligned} \eta_s(i,j) &= \sqrt{\left(\frac{\delta s}{\delta i}\cdot\tilde{\lambda}_1\right)^2 + \left(\frac{\delta s}{\delta j}\cdot\tilde{\lambda}_1\right)^2}\,, \\ \eta_t(i,j) &= \sqrt{\left(\frac{\delta t}{\delta i}\cdot\tilde{\lambda}_2\right)^2 + \left(\frac{\delta t}{\delta j}\cdot\tilde{\lambda}_2\right)^2}\,, \end{aligned} \tag{5}$$

where $\tilde{\lambda}_1$ and $\tilde{\lambda}_2$ are the mapped eigenvalues. Thus, the pattern frequency steers the perception of the field: in combination with the mapping (Eq. 2) negative eigenvalues lead to a higher frequency and allude to compression. Mapped positive eigenvalues cause a lower frequency which depicts expansion.

Color Mapping. A simple but effective way of conveying additional information is to blend color information on the input textures (Figures 4(c), 6(a),(b), and 7(b),(c)). Coloring can be applied to the eigenvector fields (one color for each field) but also according to derived scalar measures such as the magnitude of one eigenvalue, relative shear, maximum shear stress (Eq. 1), or the determinant $(\lambda_1 \cdot \lambda_2)$.

Blur by Derived Scalar Quantities. If non relevant information should be suppressed in the final image, a post-processing step can be applied to the texturized image. We employ a blur filter, but also the opacity could be modified to hide regions of low information content. Again quantities like relative and absolute shear stress come into question (Figures 6(b), and 7(b),(c)) to steer the post-processing. The pixels of the texturized image are convolved with a Gaussian kernel, where the size of the kernel is proportional to the respective value of the chosen quantity. For example, if the blur should be determined with respect to relative shear, isotropic regions are convolved with a larger kernel and anisotropic regions are convolved with a smaller kernel. Thus, regions with strongly expressed eigenvector directions are enhanced and isotropic regions blurred.

6 RESULTS

In this section, the results of the developed visualization approaches are presented and evaluated by means of two simulated datasets: the one-point load and the two-point load. The one-point load is a solid block given as a cubic volume with a single load applied to it. The two-point load is similar, just that two loads of opposing sign are applied to it. The two datasets are generated by a Finite Element Method (FEM). The methods presented above are analyzed on planar cuts of the volumetric datasets.

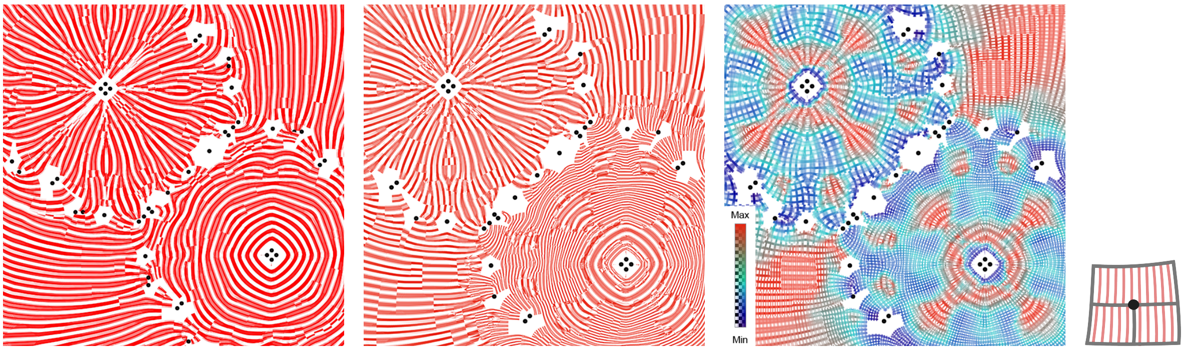

(a) (b) (c) (d)

Figure 4: Data set: Two-point load. Visualization of major eigenvector field (a) with even pattern frequency, (b) with encoded mapped eigenvalues. (c) Superposition of both eigenvector fields, color by relative shear. (d) Illustration of a hanging node.

6.1 Glyph-based Visualization

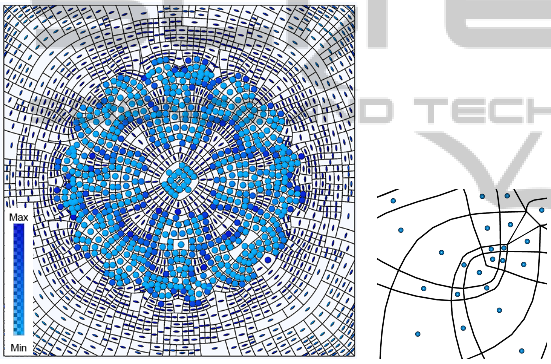

(a) (b)

Figure 5: Data set: One-point load. (a) Glyph placement in the data set. (b) Close-up of pre-computed barycentroids.

Figure 5 shows the results of the segmentation-based glyph placement (Section 5.1) applied to the one-point load. The glyphs are placed at the pre-computed barycentroids, oriented according to the eigenvectors and scaled by the mapped eigenvalues (Eq. 2). The color is assigned according to the relative shear (Eq. 1). Isotropic tensors are encoded in light blue and spherical geometries. Anisotropic tensors are encoded in dark blue and result in well-marked ellipses. This work is not concerned with elaborate glyph design or similar. With the glyph placement we rather want to provide a basis for the variety of glyphs provided in the literature (Section 2). The close-up in Figure 5(b) nicely shows how the barycentroids capture the semantic center of non-convex polygons.

6.2 Texture-based Visualization

Figure 4(a) displays the directions of the major eigenvector field. Here the basic approach of approximately constant image space line density (Section 5.2.1) is applied. Even though the textures are mapped cell-wise the continuous character of the image is harmonious. Only at transitions of cells with *hanging nodes* (Figure 4(d)) slight disruptions are noticeable. Zooming in the image automatically adapts the texture such that the stripe frequency and the even appearance is maintained. Figure 4(b) extends the representation by encoding the physical behavior. The pattern frequency is scaled by the mapped eigenvalues (Eq. 5). In the lower right corner negative eigenvalues are predominant and clearly result in a higher pattern frequency. This resembles to compressive forces and is in contrast to the upper left corner which is characterized by expansive forces. In Figure 4(c) the textures for both eigenvector fields are blended. The pattern frequency is determined again by Equation 5 and color coding is applied according to the relative shear. Isotropic regions are colored in blue and characterized by an isotropic pattern frequency. In regions of high anisotropy strongly differing eigenvalues lead to the unequal pattern frequencies for the two eigenvector fields, which is additionally emphasized by the red color.

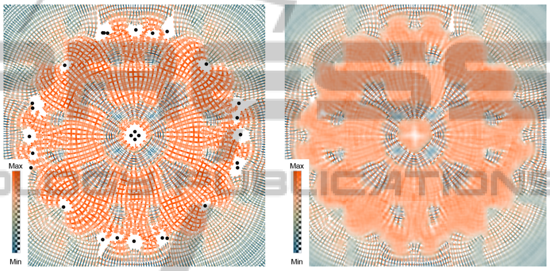

(a) (b)

Figure 6: Data set: One-point load. (a) Superposition of both eigenvector fields, color coding according to mapped eigenvalues; (b) post-processing blur by relative shear.

SCITEPRESS SCIENCE AND TECHNOLOGY PUBLICATIONS

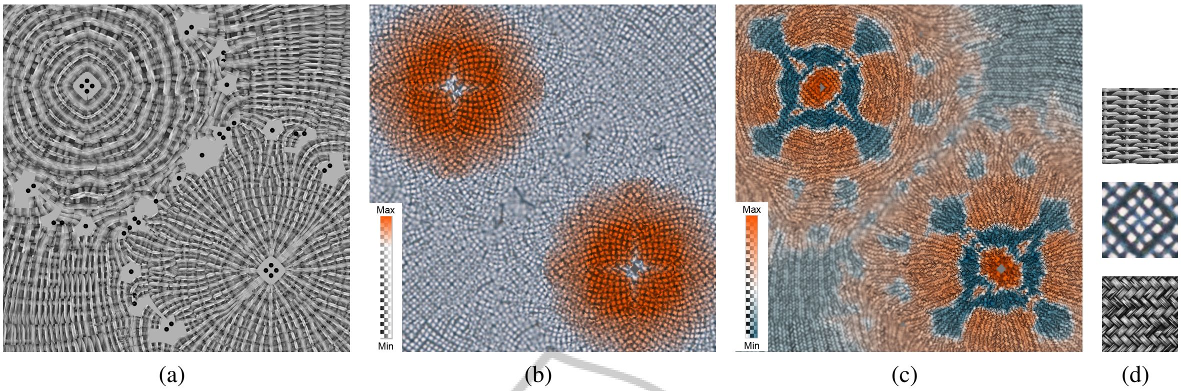

Figure 7: Data set: Two-point load. Comparison of rendering with different input textures. (a) Bidirectional weave input pattern, the frequency is adjusted to the mapped eigenvalues. (b) Rendering of the directions of maximal shear. Regions of high maximal shear stress are emphasized in red. Regions of low maximal shear are blurred. (c) Knitting pattern emphasizing major eigenvector directions from far, in detail directions of maximal shear are perceivable. Color coding is applied according to the relative shear stress. (d) Shows from top to bottom the used sample patterns in Figures (a-c).

SCITEPRESS SCIENCE AND TECHNOLOGY PUBLICATIONS

A similar visualization approach is applied to the one-point load in Figure 6(a). Here the color coding corresponds directly to the mapped eigenvalues (Eq. 2). Anisotropic regions are still discernible as the superposition generates mixed colors for strongly differing eigenvalues. Specific regions can be highlighted additionally by applying the post-processing step: in Figure 6(b) regions with low relative shear are blurred. The focus of the user is directed to anisotropic regions, where eigenvalues exhibit a large difference.

The versatility and power of textures is demonstrated in Figure 7. For texture samples with inherent natural variance discontinuities due to hanging nodes in the original segmentation are less prominent. In Figure 7(a) a weave input pattern is employed to visualize the eigenvector directions. Due to the bidirectional nature of the weave pattern both eigenvector fields are visualized at once. In Figure 7(b) the user can switch to investigate directions of maximum shear of the underlying field. Here a texture is used with line structures illustrating the bisectors of the eigenvector directions. Additionally regions of high maximal shear stress (Eq. 1) are emphasized by selective color mapping. The third example, Figure 7(c), generates a texture that resembles a knitted piece of fabric.

7 CONCLUSIONS

We have combined the accuracy of topological methods for two dimensional symmetric tensor fields with the support of more intuitive visualizations. Our approach uses the strength of textures for continuous visualizations and allows to gain insight into detailed information at discrete locations by placing glyphs. A specific topology-based segmentation framework (Auer et al., 2011) is used to employ these techniques. The cells of this segmentation provide a consistent parametrization for the texture mapping and the bounding tensorlines correctly predetermine the the eigenvector directions within. A multitude of possible textures can be implemented illustrating a harmonious continuous view on the various tensor properties. A selection of textures is presented that encode directional features; simple stripe textures but also textures with higher inherent variance, that support a smooth appearance over uneven transitions (hanging nodes). We believe the latter textures can also be used for other approaches that aim the mapping of directional textures region- oder cell-wise without apparent distorted behavior at the boundaries.
Physical properties of the tensor field like compression or expansion are reflected in the texture frequency. Selective color mapping and post processing are applied to direct the users attention to scalar features of interest. Certainly, there remains a large potential to optimally assist the perceptional habits of a user. We also presented this work as flexible basis for further advancement.

ACKNOWLEDGEMENTS

This work was funded by the German Research Foundation (DFG) through a Junior Research Group Leader award (Emmy Noether Program).

REFERENCES

Auer, C., Sreevalsan-Nair, J., Zobel, V., and Hotz, I. (to appear 2011). 2D Tensor Field Segmentation. In *Scientific Visualization: Interactions, Features, Metaphors*, volume 2 of *Dagstuhl Follow-Ups*.

Cabral, B. and Leedom, L. C. (1993). Imaging Vector Fields Using Line Integral Convolution. In *Proc. of the 20th annual conference on Computer graphics and interactive techniques*, pages 263–270.

Delmarcelle, T. (1994). *The Visualization of Second-order Tensor Fields* . PhD thesis, Stanford University.

Delmarcelle, T. and Hesselink, L. (1993). Visualization of Second Order Tensor Fields and Matrix Data. *IEEE Computer Graphics & Applications*, pages 25–33.

Dick, C., Georgii, J., Burgkart, R., and Westermann, R. (2009). Stress Tensor Field Visualization for Implant Planning in Orthopedics. *IEEE Transactions on Visualization and Computer Graphics*, 15(6):1399–1406.

Feng, L., Hotz, I., Hamann, B., and Joy, K. (2008). Anisotropic Noise Samples. *IEEE Transactions on Visualization and Computer Graphics*, 14(2):342–354.

Hashash, Y. M. A., Yao, J. I.-C., and Wotring, D. C. (2003). Glyph and Hyperstreamline Representation of Stress and Strain Tensors and Material Constitutive Response. *Int. Journal for Numerical and Analytical Methods in Geomechanics*, 27(7):603–626.

Hesselink, L., Levy, Y., and Lavin, Y. (1997). The Topology of Symmetric, Second-Order 3D Tensor Fields. *IEEE Transactions on Visualization and Computer Graphics*, 3(1):1–11.

Hlawitschka, M., Scheuermann, G., and Hamann, B. (2007). Interactive Glyph Placement for Tensor Fields. In *ISVC (1)*, pages 331–340.

Hotz, I., Feng, L., Hagen, H., Hamann, B., Jeremic, B., and Joy, K. (2004). Physically Based Methods for Tensor Field Visualization. In *Proc. of IEEE Visualization (Vis'04)*, pages 123–130.

Hummel, M., Garth, C., Hamann, B., Hagen, H., and Joy, K. I. (2010). IRIS: Illustrative Rendering for Integral Surfaces. *IEEE Transactions on Visualization and Computer Graphics*, 16:1319–1328.

Kindlmann, G. and Westin, C.-F. (2006). Diffusion Tensor Visualization with Glyph Packing. *IEEE Transactions on Visualization and Computer Graphics*, 12(5):1329–1336.

Kratz, A., Kettlitz, N., and Hotz, I. (2011). Particle-Based Anisotropic Sampling for Two-Dimensional Tensor Field Visualization. In *Vision Modeling and Visualization (VMV'11)*, pages 145–152.

Lavin, Y., Batra, R., Hesselink, L., and Levy, Y. (1997). The Topology of Symmetric Tensor Fields. *AIAA Computational Fluid Dynamics Conference,*, page 2084.

Rustamov, R. M., Lipman, Y., and Funkhouser, T. (2009). Interior Distance Using Barycentric Coordinates. In *Proc. of the Symposium on Geometry Processing (SGP '09)*, pages 1279–1288.

Schultz, T. and Kindlmann, G. (2010). Superquadric Glyphs for Symmetric Second-Order Tensors. *IEEE Transactions on Visualization and Computer Graphics*, 16:1595–1604.

Sreevalsan-Nair, J., Auer, C., Hamann, B., and Hotz, I. (2010). Eigenvector-based Interpolation and Segmentation of 2D Tensor Fields. In *Topological Methods in Visualization. Theory, Algorithms, and Applications (TopoInVis 2009)*.

Tricoche, X., Kindlmann, G. L., and Westin, C.-F. (2008). Invariant Crease Lines for Topological and Structural Analysis of Tensor Fields. *IEEE Transactions on Visualization and Computer Graphics*, 14(6):1627–1634.

Tricoche, X., Scheuermann, G., Hagen, H., and Clauss, S. (2001). Vector and Tensor Field Topology Simplification on Irregular Grids. In *Proceedings of the Symposium on Data Visualization (VisSym '01)*, pages 107–116.

Zheng, X. and Pang, A. (2003). HyperLIC. In *Proc. of IEEE Visualization (Vis'03)*, pages 249–256.

Zheng, X. and Pang, A. (2004). Topological Lines in 3D Tensor Fields. In *Proc. of IEEE Visualization (Vis'04)*.

SCITEPRESS SCIENCE AND TECHNOLOGY PUBLICATIONS